Electrowetting of Superhydrophobic ZnO Inverse Opals

Li-Yin Chen, Chun-Han Lai, Pu-Wei Wu,[z,*] and Shih-Kang Fan

Department of Materials Science and Engineering, National Chiao Tung University, Hsin-Chu 300, Taiwan

ZnO inverse opals are fabricated by electrophoresis of polystyrene (PS) microspheres (720 nm in diameter) on a ITO glass to form a close-packed colloidal crystal, followed by potentiostatic deposition of ZnO in the interstitial voids among the PS microspheres and chemical removal of the PS colloidal template. By adjusting the electrodeposition time, we obtain semi-layered and multi-layered ZnO inverse structures with significantly reduced defects and considerable surface uniformity. The semi-layered ZnO inverse opals display a bowl-like morphology with individual cavities isolated from each other. In contrast, the multi-layered ZnO inverse opals exhibit a three-dimensional skeleton with hexagonally-arranged cavities interconnected to each other. After surface coating of perfluorodecyltriethoxysilane, both samples reveal a superhydrophobic nature with contact angle larger than 150°. In electrowetting measurements, the contact angles are decreasing with increasing applied voltages. The droplet on the semi-layered ZnO inverse opals demonstrates a notable transition from the Cassie-Baxter state to the Wenzel one. However, the droplet on the multi-layered ZnO inverse opals indicates three distinct regimes; Cassie-Baxter state, mixed Cassie-Baxter/Wenzel state, and Wenzel state. Repelling pressure of the entrapped air in the cavities is estimated to explain the observed contact angle variation upon the applied voltage for both samples.
© 2011 The Electrochemical Society. [DOI: 10.1149/1.3594723] All rights reserved.

The surface property for a solid material can be deliberately controlled from hydrophilic to hydrophobic in order to affect the wetting behavior of a water droplet that is in contact with the solid surface. So far, external stimuli such as electric field, mechanical force, magnetic field, electrochemical reaction, and photon excitation have been employed to manipulate physical and chemical attributes of the surface.[1–5] Among them, the electrical route, known as electrowetting (EW), is recognized for its fast response, reversibility, and compatibility with microdevices.[6–8] To date, the implementation of EW for applications such as microfluidics and optoelectronic components have been explored.[9–11] In EW, the water droplet on the solid surface reveals a significant morphological alteration from a large contact angle (hydrophobic) to a reduced one (hydrophilic) upon the imposition of voltage across the solid surface and water droplet. This is because the electrical field engenders a capacitive charging on the interface that increases its surface energy considerably. As a result, the water droplet is able to wet the solid surface lowering the overall interfacial energy.

For a desirable EW material, a large contact angle at zero voltage and a stronger capacitive effect are always preferred. To achieve these objectives, recent research attention has focused on the design and fabrication of one-dimensional materials such as nanowires and nanorods.[12–15] In general, the wetting behavior for the water droplet on a nanostructured surface can be categorized in Cassie-Baxter model or Wenzel model.[16,17] In the Cassie-Baxter model, the water droplet is supported merely by the tip of the nanostructure that is in contact directly with the liquid leaving air entrapped underneath. In contrast, in the Wenzel model, the nanostructure is completely submerged in the water droplet so the entire surface is wetted. It is realized that the water droplet atop a superhydrophobic surface, defined when the contact angle is larger than 150°, often adopts the Cassie-Baxter state, as evidenced by many laboratory demonstrations and biological structures like lotus leaf and legs of water strider.[18,19] In addition, reversibility in the EW is observed for the Cassie-Baxter state as the water droplet is able to move relatively freely unlike that of Wenzel state in which the water droplet becomes immobile as it descends into the nanostructure.

The EW response can be further enhanced by inserting a dielectric layer such as flouropolymers in between a conductive layer underneath and a hydrophobic coating atop.[20] Under the applied voltage, this composite structure reveals a significantly enhanced EW response, known as electrowetting-on-dielectric (EWOD). In 2002, Lee et al. first conducted EWOD experiments on a patterned electrode for microscale liquid handling.[21] Afterward, in 2004, the study of EWOD was carried out on a nanostructured surface by Krupenkin et al. using flouropolymer-coated silicon nanorods, in which the droplet was switched rapidly from a superhydrophobic state to superhydrophilic one.[22] Later in 2006, Dhindsa et al.[23] demonstrated a reversible EWOD on the carbon nanofibers coated with alumina and paraylene, and determined that the sensitivity of EWOD was affected by their respective dielectric constants. To date, research activities on the EWOD have produced impressive progresses and relevant information can be found in several review papers.[24–27]

Zinc oxide (ZnO) is a low-cost semiconductor with direct wide band gap (3.36 eV at room temperature) and large exciton binding energy (60 mV).[28] Because the ZnO exhibits notable chemical stability and biological compatibility, it has attracted significant attention for applications in photocatalysis, electronics, optoelectronics, and sensors.[29–32] So far, many forms of ZnO have been fabricated and evaluated for wetting properties.[14,15,33–35] Previously, Papadopoulou et al.[36] investigated the nanostructured ZnO films, and determined that the bias necessary to actuate the EW behavior was negligible. In addition, the nanostructured film exhibited a strong sensitivity to the applied voltage, which was attributed to the oxygen vacancies intrinsic in the ZnO lattice. Similar work was carried out by Campbell et al. on the ZnO nanorods, and their EWOD behaviors were compared with those of carbon nanotubes, carbon nanofibers, and silicon nanostructures.[15]

As compared to the one-dimensional nanorods, the inverse opals demonstrate a three-dimensional periodic skeleton with adjustable pore size and thickness, which enables a large surface area with interconnected channels. As a result, the EWOD behaviors for the inverse opals might be of potential interests for photonic and electrochemical reactions. Recently, we have reported the fabrication of large-area colloidal crystals and their inverse opals at controlled thickness by electrophoresis and electrodeposition.[37,38] In particular, we demonstrate the formation of ZnO inverse opals with uniform surface morphology and reduced crystallographic defects.[39] In this work, we prepare the ZnO inverse opals in both semi-layered and multi-layered thickness and evaluate their respective EWOD behaviors.

Experimental

The ZnO inverse opals were fabricated by electroplating of ZnO in a PS colloidal crystal followed by chemical removal of the PS template. To prepare the colloidal crystal, PS microspheres were synthesized via an emulsifier-free emulsion polymerization process in which the styrene and $K_2S_2O_8$ were used as the monomer and

* Electrochemical Society Active Member.
z E-mail: ppwu@mail.nctu.edu.tw

inhibitor, respectively. First, 0.25 g NaHCO$_3$ was dissolved in 300 ml deionized water under nitrogen atmosphere at 65°C. Subsequently, 40 ml styrene and 0.25 g K$_2$S$_2$O$_8$ were added allowing the polymerization to take place. After 18 h, we obtained the PS microspheres of 720 nm in diameter with a standard deviation of 16.7 nm. Electrophoresis of PS microspheres was carried out to prepare the colloidal crystal. A stable suspension was formed by mixing 0.5 g PS microspheres in 100 ml ethanol (99.5 vol %) with pH adjusted to 8.2. An ITO glass (1×1 cm) and stainless steel (5×5 cm) were employed as the working and counter electrode, respectively. An electric field of 3 V/cm was imposed for 15 min at 26°C to render a PS template with 6.56 μm thickness. Afterward, the PS template was carefully removed and dried in air at 50°C for 10 min. In ZnO electrodeposition, the PS template was served as the working electrode, and a zinc plate (5×5 cm) was used as the counter electrode. A potentiostatic plating at -1 V (vs. Ag/AgCl) was conducted at 65°C in 0.05 M ZnSO$_4$ aqueous solution to deposit the ZnO in the interstitial voids among the PS microspheres. The plating time was adjusted to obtain ZnO deposit with different thickness (layers). Upon finished, the sample was cleaned with deionized water and the PS template was chemically removed by immersion in an ethyl acetate solution (95 vol %) at 25°C for 3 h leaving an integral ZnO inverse structure. To render the ZnO skeleton a hydrophobic nature, the sample was submerged in a methanol solution containing 1 wt % perfluorodecyltriethoxysilane (FAS-17) at 25°C for 10 h to ensure sufficient adsorption of the water-repelling compound.

In the EWOD measurements, the ZnO structure was served as a dielectric layer sandwiched between the conducting ITO glass underneath and hydrophobic FAS-17 above. A 2 μl water droplet with 0.78 mm in radius was positioned atop the ZnO inverse opals. The droplet contained 0.05 M KCl for conductivity enhancement. During the testing, an ac sinusoidal voltage of 1 kHz was imposed across the droplet (tungsten electrode) and ITO glass from 0 to 43.4 V (root-mean-square voltage) at 2 V/s. A camera coupled with light source was located nearby to capture the morphology for the droplet at various applied voltages, and the resulting contact angles were determined via a personal computer and an image processing software. A schematic for the measurement setup is depicted in Fig. 1. A scanning electron microscope (SEM, JEOL-JSM-600F) was used to observe the microstructure for the ZnO inverse opals in top and cross-sectional views.

Results and Discussion

Figure 2 provides the SEM images for the ZnO inverse opals after surface coating of FAS-17 in both top and cross-sectional views. As shown in Fig. 2a, the ZnO sample was obtained via an electrode-
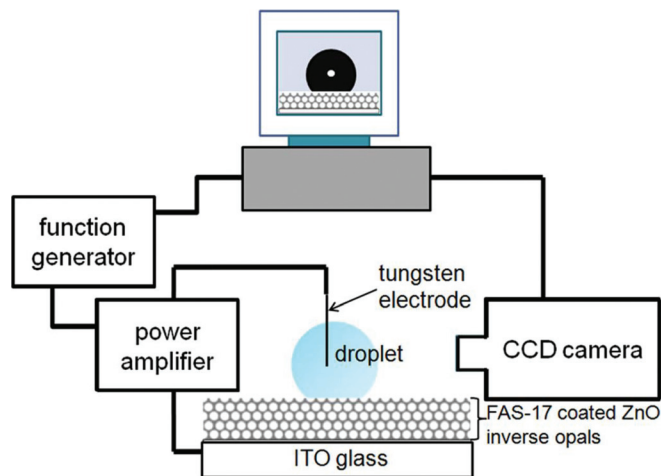

Figure 1. (Color online) Measurement setup in EWOD experiments for droplets on ZnO inverse opals.
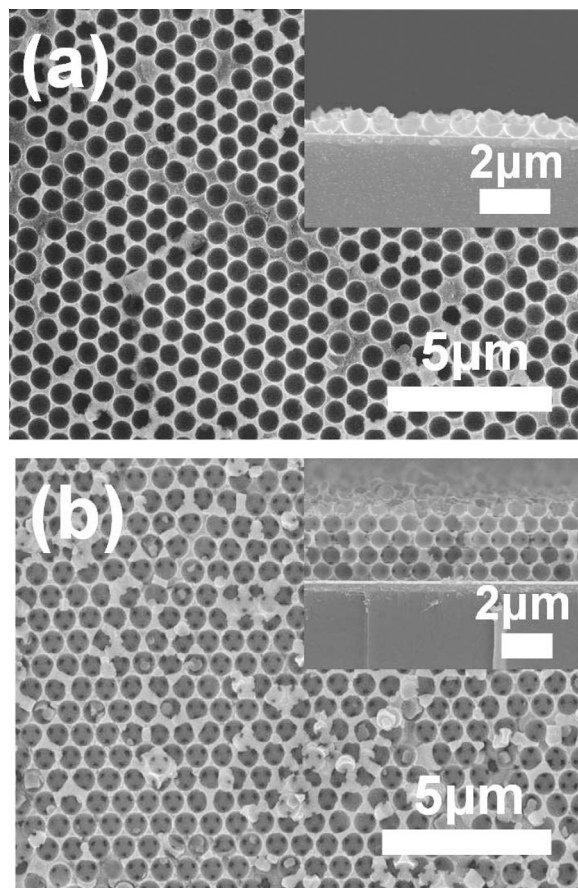

Figure 2. SEM images for ZnO inverse opals after electrodeposition at -1 V (vs. Ag/AgCl) for (a) 1 and (b) 7 min. Insets are their respective cross-sectional SEM images.

position for 1 min, rendering a ZnO thickness of 0.38 μm, which corresponded to 0.5 inverse opaline layer. From the top view, the ZnO inverse opals displayed an ordered array of hexagonally-arranged pores. In addition, the surface morphology was relatively smooth without notable protrusion and disconnected islands, indicating that the PS microspheres were nicely assembled in electrophoresis so the following electroplating process was able to occur uniformly at a controlled rate across the entire 1×1 cm sample area. From the cross-sectional view, the semi-layered ZnO inverse opals demonstrated a bowl-like morphology with periodic cavities replicating the removed PS microspheres and individual pillars were formed in the interstitial sites.

Figure 2b exhibits the multi-layered ZnO inverse opals obtained from an electrodeposition for 7 min. Its thickness was 2.91 μm, which corresponded to 4.5 inverse opaline layer. It can be seen that with increasing deposition time, the ZnO structure evolved from individual cavities to a multi-layered skeleton with interconnected channels. Notably, this multi-layered inverse structure displayed a similar surface morphology like the semi-layered one. Since the PS microspheres were in a fcc close-packed configuration with 12 nearest neighbors, each PS microsphere had six neighbors on the same plane plus three neighbors above and three neighbors below. As the ZnO was not deposited in the contacting areas between neighboring PS microspheres, these contacting areas became channels connecting cavities left by the removed PS microspheres. From the SEM image, the diameter for the circular channels was 138.8 nm. This is different from the semi-layered ZnO inverse opals where each cavity was isolated entirely from each other. This distinction is expected to reveal a notable effect on the EWOD when a droplet is forced to descend into the ZnO inverse opals.

Figure 3 presents the optical pictures for the 2 μl droplet on the ZnO inverse opals at various applied voltages. It is known that when the length scales for the droplet and nanostructured surface are in micrometer regimes, the gravity effect on the contact angle is negligible and the surface tension becomes the dominant force in determining the wetting behavior for the droplet. As shown in Fig. 3, both samples revealed decreasing contact angles with increasing applied voltages, a typical behavior for EWOD. For the semi-layered ZnO inverse opals shown in Fig. 3a, a contact angle of 161.5° at zero voltage was observed. In our experiments, a planar ZnO film prepared by identical electrodeposition route exhibited a contact angle of 107° and after FAS-17 coating, its contact angle was increased to 122.2°. In contrast, for the ZnO inverse opals, a contact angle of 119.4° was observed before the FAS-17 coating. Previously, Campbell et al. fabricated the ZnO nanorods using a hydrothermal process and reported a contact angle of 155° after hydrophobic treatment.[15] Similarly, Badre et al. synthesized the ZnO nanowires by electrodeposition and determined a contact angle of 176°.[33] Apparently, our contact angle was in the same range like theirs after the hydrophobic treatment. This notable superhydrophobicity for the semi-layered ZnO inverse opals was attributed to both the bowl-like structure and FAS-17. We realized that the droplet was present in a Cassie-Baxter state, i.e., the droplet was supported by the pillar and entrapped air underneath simultaneously.

Figure 3b demonstrates the EWOD behavior of the multi-layered ZnO inverse opals. From Fig. 2, we concluded that the surface morphology was rather similar between the semi-layered and multi-layered ZnO inverse opals. Therefore, at zero voltage, their contact angle was likely to be identical. Indeed, we observed a contact angle of 158.6° for the multi-layered sample, which was close to the 161.5° from the semi-layered one. In addition, both samples revealed a reduced sliding angle of less than 5°. This inferred that the droplet also adopted the Cassie-Baxter state. These behaviors were expected as the FAS-17 was able to form a continuous film on the inverse structure because a similar practice was performed previously by Li et al. using the FAS-17 for hydrophobic treatment on the electrodeposited ZnO film.[40] In our case, the formation of FAS-17 was substantiated by the F1s signal from the X-ray photoelectron spectroscope.

According to literature, in the Cassie-Baxter state at zero voltage, the contact angle for the droplet on a nanostructured surface $(\cos\theta_c)$ can be derived from the apparent contact angle on the planar counterpart $(\cos\theta_0)$ by the following equation[25]

$$(\cos\theta_c) = -1 + \varphi + \varphi\cos\theta_0 \qquad [1]$$

where φ is the ratio for the effective liquid-solid surface to the total planar surface. In our experiments, the θ_0 was recorded at 122.2°. Figure 4 illustrates the schematic for the inverse opals in top and cross-sectional views. In the drawing, R is the distance from the cavity center to the center of ZnO skeleton, r is the cavity radius, and s is the radius for the channels among individual cavities. As shown, the φ represents the highlighted area divided by the area of

Figure 3. Optical images for droplets (2 μL) in progressive applied voltages on (a) semi-layered and (b) multi-layered ZnO inverse opals.

hexagonal unit cell. In the Cassie-Baxter state, the droplet was merely sitting on the exterior surface but not touching on the interior area of the cavity. Hence, the s was not expected to contribute to the calculation of φ. As a result, the φ can be simply determined by the following relation

$$\varphi = 1 - \frac{\pi\sqrt{3}r^2}{6R^2} \qquad [2]$$

A close examination on the SEM images in Fig. 2 concluded the values for R, r, and s were 360, 348, and 69 nm, respectively. Since both the semi-layered and multi-layered ZnO inverse opals displayed similar surface morphologies, the φ was kept at 0.152. Consequently, according to Eq. 1 the theoretic θ_c for both samples was expected to be 155.8°, a value reasonably close to our experimentally determined values of 161.5 and 158.6° for the semi-layered and multi-layered ZnO inverse opals. For an ideal colloidal crystal, individual microspheres are contacting each other in a close-packed arrangement, leading to identical values of R and r. In such case, the φ becomes 0.093, resulting in an ideal contact angle of 163.1°. Interestingly, our experimentally determined values were close to the predicted values from an ideal inverse structure. According to Eq. 1, the φ is a critical factor in determining the θ_c for a nanostructured surface. For an ideal inverse structure regardless the material that makes up the skeleton, the φ is always fixed at 0.093 because of the constraint by the close-packed assembly of microspheres. However, in practical cases for other nanostructured surfaces, the θ_c can be varied considerably contingent on the structure density.

Figure 5 presents the variation of contact angle as a function of applied voltage and Fig. 6 provides the illustrations for the droplet in different states on both samples. Apparently, the contact angle was reduced continuously with increasing applied voltage. For the semi-layered ZnO inverse opals, the droplet exhibited a slowly decreasing contact angle until a threshold voltage of 26 V. Afterward, a rapidly declining contact angle was observed until 35 V where the droplet descended completely to the cavities, engendering water electrolysis that destroyed the FAS-17 and ZnO skeleton. We realized that the threshold voltage of 26 V indicated the transformation from the Cassie-Baxter state to the Wenzel state. The respective slope before and after 26 V was −0.39 and −6.65°/V. Since the electroplated ZnO often contains notable defects identified as oxygen vacancies, a large capacitance is expected under external bias that draws the droplet into the interior area of the ZnO skeleton. Despite the relatively larger capacitance expected for the ZnO inverse opals, the variation of contact angle before 26 V was rather moderate. For example, in literature, the ZnO nanorods and nanowires revealed slopes of −1.95 and −0.9°/V in the Cassie-Baxter state, respectively.[15,41] This subdued slope in our case is attributed to the entrapped air in isolated cavities that is unable to escape. In contrast, in typical nanorods or nanowires, air motion underneath is not inhibited so the droplet is likely to descend with less resistance.

For the multi-layered ZnO inverse opals, there appeared two threshold voltages at 14 and 32 V, respectively. Before 14 V, the droplet was in the Cassie-Baxter state, and between 14 and 32 V, the droplet adopted a mixed Caxie-Baxter and Wenzel state instead. When the voltage reached 32 V, the droplet transformed to the Wenzel state. The respective slopes for these three regimes were −0.36, −1.31, and −3.39°/V. For both samples in the initial Cassie-Baxter state, their slopes were rather close which was understandable as the multi-layered ZnO inverse opals demonstrated a similar surface morphology to that of semi-layered one. The appearance of mixed state for the multi-layered ZnO inverse opals is quite interesting. Since the multi-layered ZnO inverse opals not only allow additional depth for the droplet to descend but also produce more areas for capacitive charging, the droplet is likely to penetrate halfway filling up the top cavities, leaving the trapped air underneath. As a result, the droplet is simultaneously supported by the entire wetting area on the top cavity and entrapped air at the bottom. The presence of meta-stable mixed state is unusual as many earlier reports always
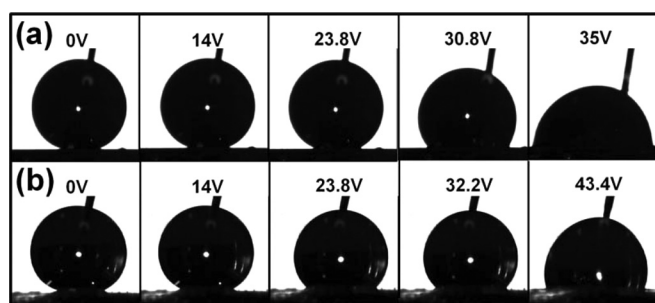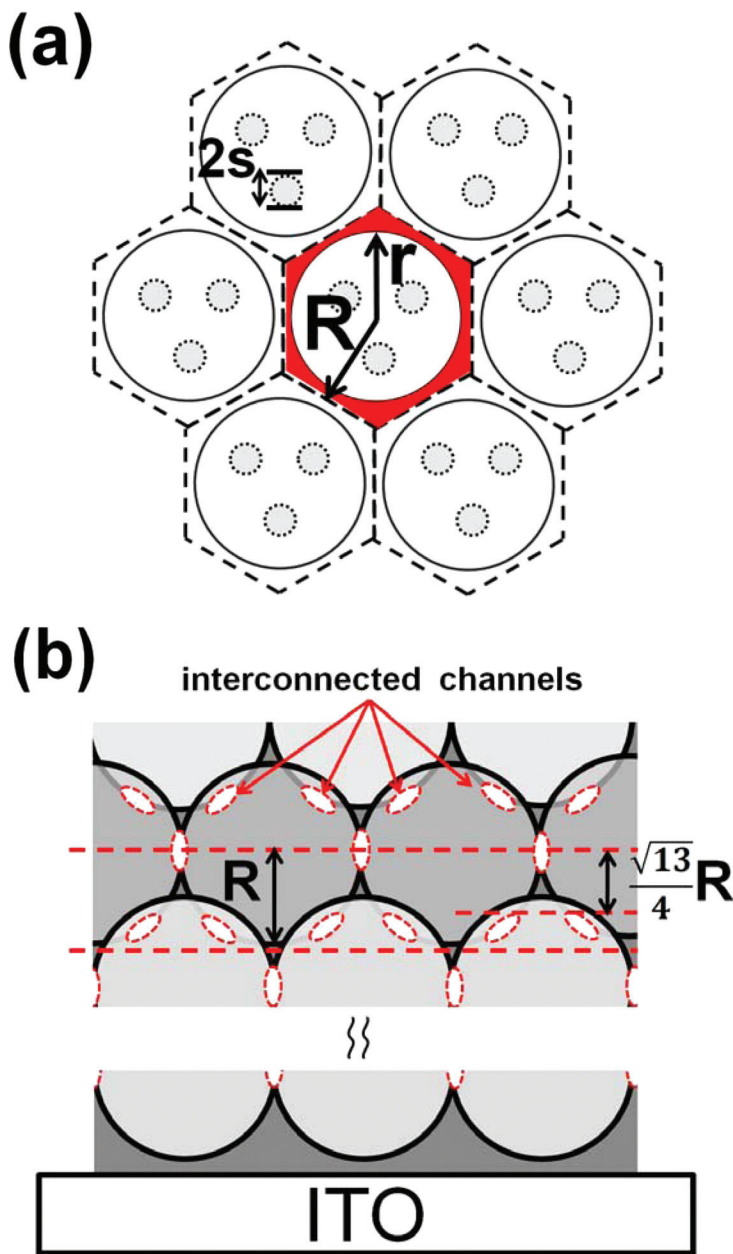
Figure 4. (Color online) Schematics for ZnO inverse opals in top and cross-sectional views.

suggested a two-stage transition for the droplet on a nanostructured surface.[17,22,23,25,41–43]

In EWOD, the threshold voltage represents the critical driving force to drag the droplet into the inverse opals, and this driving force is counteracted by the pressure of entrapped air. At a sufficiently large voltage, the droplet is able to overcome the repelling force to wet the interior of the cavity. Therefore, estimation of the repelling pressure provides insightful information for the contact angle variation upon various applied voltages and consequently the droplet state on the surface. It is realized that once the droplet descends into to the cavity for certain depth, the volume for the entrapped air would be reduced significantly. For the semi-layered inverse opals, individual cavities are isolated from each other so the ideal gas law is applicable. As shown in Fig. 7a, the repelling pressure for the entrapped air (P_c) is a function of the penetration depth (h) for the droplet, atmospheric pressure (P_0), and the distance from the cavity center to the center of ZnO skeleton (R)

$$P_c = \frac{3P_0}{[\pi(2R^3 - 3(h+92)R^2 + (h+92)^3)]} \qquad [3]$$

where P_0 is 0.1 MPa (1 atm) and R is 360 nm.

In contrast, for the multi-layered ZnO inverse opals, individual cavities are connected by channels to allow unrestricted air flow. Hence, the Young-Laplace relation is more pertinent to estimate the repelling pressure. As shown in Fig. 7b, the Young-Laplace pressure (P_y) for the droplet is given by[44]

$$P_y = |2\gamma_{la}\cos\theta_0/R_c| \qquad [4]$$
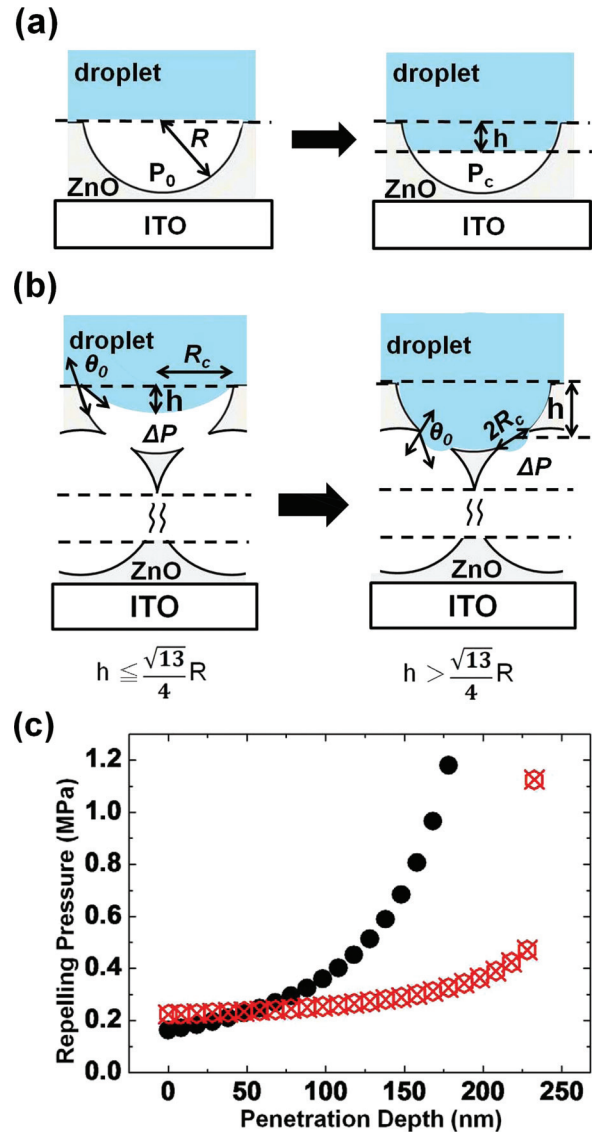
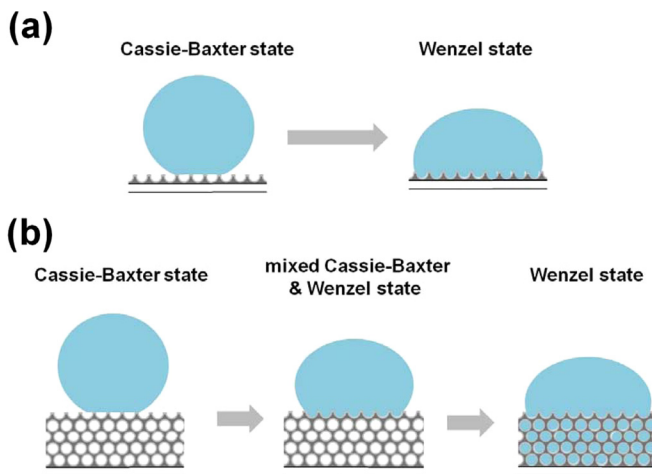and from geometric consideration we know

$$R_c = \sqrt{R^2 - (h+92)^2} \qquad [5]$$
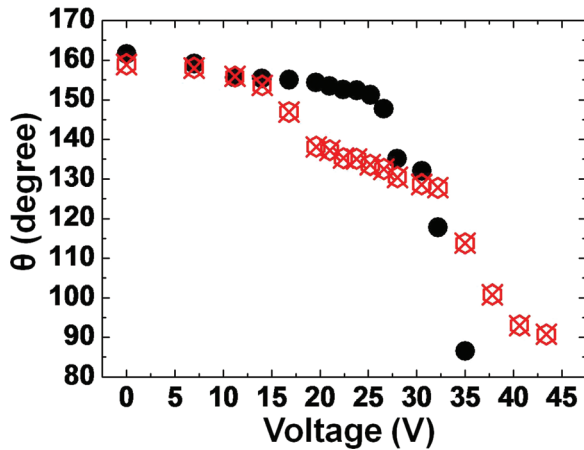
Figure 5. (Color online) Variation of contact angle (θ) as a function of applied voltage (V) for droplets on semi-layered (●) and multi-layered (⊠) ZnO inverse opals.

Figure 7. (Color online) Schematics for water meniscus on (a) semi-layered and (b) multi-layered ZnO inverse opals. (c) Profiles of repelling pressure by entrapped air as a function of droplet penetration depth (h) on semi-layered (●) and multi-layered (⊠) ZnO inverse opals.

where R_c is the curvature of water meniscus inside the cavity, and γ_{la}(72.8 mN/m) is the surface tension of liquid-air interface. The R, h, and θ_0 are defined previously.

Figure 7c presents the estimation of repelling pressure as a function of h for both samples. For the semi-layered ZnO inverse opals, apparently the increment of h induces a steady rise of repelling pressure followed by an accelerated increase when the h becomes larger than 180 nm. In contrast, for the multi-layered ZnO inverse opals, there appears a relatively unchanged repelling pressure until a sudden increase when the h reaches 237 nm. This large repelling pressure occurs when the water meniscus descends to the interconnecting channels between neighboring cavities. At this stage, the R_c is equivalent to the radius of the channels which is 69 nm, and the critical h is 237 nm. Comparing the profiles for both samples, the repelling pressure for the semi-layered inverse opals is always larger than that of multi-layered one, suggesting a higher threshold voltage is necessary for the droplet to wet the semi-layered inverse opals, a fact supported by earlier observations shown in Fig. 5. An alternative explanation for the larger repelling pressure is the "overhang structure" on the surface of semi-layered inverse opals, which can be seen from Fig. 2a. According to literature, the water droplet requires a substantially higher hydrostatic pressure in order to penetrate to the gaps between these structures.[45,46] Since the ZnO inverse opals in our case are not perfectly flat, the presence of local protru-

sions is likely resulting in the formation of "overhang" structure that increases the repelling pressure.

In addition to the repelling pressure, Fig. 7c also infers the state of transition for both samples. The semi-layered ZnO inverse opals experience a well-defined transition from the Cassie-Baxter state to the Wenzel state because the invasion of water into air cavity is rather difficult as there is no escape route for the entrapped air. In contrast, the repelling pressure for the multi-layered inverse opals shows a steady increase with the penetration depth. At 237 nm, this sudden increase of repelling pressure is resulted from the Young-Laplace equation for the meniscus reaching the interconnected channels, which is estimated at 1.124 MPa from Eq. 4. This infers that a transition state is possible between these two repelling pressure for the multi-layered ZnO inverse opals.

To fully interpret the EWOD behaviors, the Lippmann-Young equation was applied in the Cassie-Baxter and Wenzel states. Figure 8 presents the cosθ versus the applied voltage square for the droplets on both samples. For the Cassie-Baxter state, the variation from the initial contact angle at zero voltage (θ_c) to the contact angle under the applied voltage (θ_c^E) is given by[36]

Figure 6. (Color online) Schematics for droplets on (a) semi-layered and (b) multi-layered ZnO inverse opals at various applied voltages.

$$\cos \theta_c^E = \cos \theta_c + \varphi k V^2 \qquad [6]$$

$$k = \varepsilon \varepsilon_0 / (2d\gamma_{la}) \qquad [7]$$

where φ is defined previously, ε_0 is the vacuum permittivity (8.854×10^{-12} C^2/N-m), ε is the dielectric constant of ZnO, and d is the thickness for the ZnO inverse opals. Hence, we calculated the slopes of the curves by Eq. 6 using $\varphi = 0.152$, $\varepsilon = 8$ for the ZnO,[47] $\gamma_{LA} = 72.8$ dyne/cm for 0.05 M KCl solution,[48] as well as d = 0.38 μm (semi-layered) and d = 3 μm (multi-layered). We determined that the k was 1.289×10^{-3}, for semi-layered inverse opals and 1.578×10^{-3} for multi-layered inverse opals, and the theoretic slopes (φk) were 1.96×10^{-3} and 2.4×10^{-4} [V^{-2}] for the semi-layered and multi-layered inverse opals, respectively. In contrast, the experimental slopes from curve-fitting of Fig. 8 in the Cassie-Baxter state for the semi-layered and multi-layered samples were 9×10^{-5} and 2×10^{-4} [V^{-2}], respectively. Interestingly, we obtained reasonable agreement between the theoretic estimation and experimentally determined value for the multi-layered ZnO inverse opals. However, there was a significant deviation between these two values for the semi-layered ZnO inverse opals. We rationalized that for the semi-layered inverse opals, the air entrapped in the cavity was immobile which is different from the boundary conditions pertinent to the derivation of Lippmann-Young equation. Because the repelling pressure was not released, a stronger applied voltage became necessary to drive the droplet downward.

After the threshold voltage was attained, the droplet wetted the ZnO skeleton and its behavior followed the Wenzel model. The slope obtained from the curve was 1.6×10^{-3} [V^{-2}] for the semi-layered sample. In addition, for the multi-layered inverse opals, the slope became 2×10^{-4} [V^{-2}] in the mixed state of Cassie-Baxter and Wenzel, and 9×10^{-4} [V^{-2}] in the Wenzel state. In the mixed state of Cassie-Baxter and Wenzel, the droplet started wetting the top cavity gradually, with its contact angle decreased from 153.6° (14 V) to 138.2° (19.6 V). This notable reduction in the contact angle was also observed for silicon nanorods[22] and ZnO nanostructures[49] when the droplet was dragged partially to the bottom. In our case, the slope for the mixed Cassie-Baxter and Wenzel state was similar to that of the previous Cassie-Baxter state because the dragging force for the droplet competed against the repelling Young-Laplace pressure.

According to literature, in the Wenzel state the variation of contact angle (θ_w^E) under the applied voltage can be given by the following equation[42]
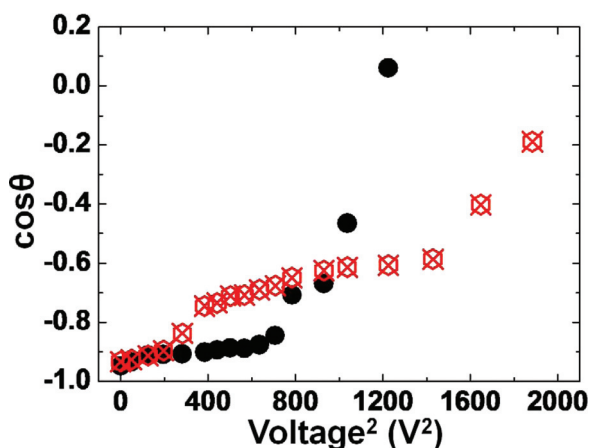
$$\cos \theta_w^E = \cos \theta_w + rk V^2 \qquad [8]$$

Figure 8. (Color online) Plots of cosθ as a function of applied voltage square (V^2) for droplets on semi-layered (•) and multi-layered (⊠) ZnO inverse opals.

where r and k are defined previously, and θ_w is the contact angle for the Wenzel state at zero voltage. Unfortunately, for both samples the variation of θ_w^E were inconsistent with what was predicted from Eq. 8. This behavior was possibly resulted from the leakage current as earlier work by Barberoglou et al.[50] observed the saturation of contact angle, and they determined the leakage current increased as a function of applied voltage. Since the FAS-17 coating on the ZnO skeleton was expected to be mono-layered, the presence of defects was certainly likely. As a result, under a sufficiently large bias, the leakage current became noticeable that led to the deviation from theoretic prediction.

It is noted that the sessile drop method is adopted in our work to record the variation in the Young's contact angle (θ_c^E and θ_w^E) under an increasingly applied voltage. In addition, by deviation from an ideal quadratic curve, we determine the voltage that initiates the transition between Cassie-Baxter and Wenzel states for both semi-layered and multi-layered ZnO inverse opals. In literature, an alternative approach to explore the EW behaviors is to measure the advancing and receding angles at various applied voltages.[51,52] The difference between the advancing and receding contact angles is known as the contact angle hysteresis and a transition between the Cassie-Baxter and Wenzel states is expected to render a substantial changeup in the contact angle hysteresis. However, in our sessile drop method, the Young's contact angle is approximately equivalent to the advancing angle so by directly observing its variation upon applied voltages, the transition between wetting states can be determined.

Conclusions

We prepared the ZnO inverse opals by electrophoresis of PS microspheres in a close-packed assembly followed by electrodeposition of ZnO and chemical removal of the PS template. By varying the ZnO deposition time, we obtained semi-layered and multi-layered ZnO inverse opals with reduced defects. SEM images indicated a bowl-like structure with individual cavities isolated from each other for the semi-layered ZnO sample. In contrast, the multi-layered ZnO sample displayed a three-dimensional skeleton with periodic cavities interconnected to each other. After coating of FAS-17, both samples revealed a superhydrophobic nature where the water droplet adopted the Cassie-Baxter state. In EW, with increasing applied voltage, the contact angles were decreasing as expected. The droplet on the semi-layered ZnO inverse opals demonstrated a clear transition at 26 V from the Cassie-Baxter state to the Wenzel state. However, the droplet on the multi-layered ZnO inverse opals showed three distinct regimes; Cassie-Baxter state (< 14 V), mixed Cassie-Baxter and Wenzel state (14–32 V), as well as Wenzel state (> 32 V). Repelling pressure of the entrapped air in the cavities was estimated and used to explain the respective contact angle variation upon the applied voltage for both samples. In addition, the Lippmann-Young equation was applicable only for the multi-layered ZnO inverse opals in the Cassie-Baxter state.

Acknowledgment

References

1. W. J. W. Welters and L. G. J. Fokkink, *Langmuir*, **14**, 1535 (1998).
2. A. Lafuma and D. Quéré, *Nature Mater.*, **2**, 457 (2003).
3. X. Hong, X. Gao, and L. Jiang, *J. Am. Chem. Soc.*, **129**, 1478 (2007).
4. C. Badre and T. Pauporté, *Adv. Mater.*, **21**, 697 (2009).
5. R. D. Sun, A. Nakajima, A. Fujishima, T. Watanabe, and K. Hashimoto, *J. Phys. Chem. B*, **105**, 1984 (2001).
6. K. H. Kang, *Langmuir*, **18**, 10318 (2002).
7. H. J. Moon, S. K. Cho, R. L. Garrel, and C. J. Kim, *J. Appl. Phys.*, **92**, 4080 (2002).
8. C. W. Monroe, M. Vrbakh, and A. A. Kornyshev, *J. Electrochem. Soc.*, **156**, P21 (2009).
9. M. G. Pollack, R. B. Fair, and A. D. Shenderov, *Appl. Phys. Lett.*, **77**, 1725 (2000).

10. S.-K. Fan, H.-P, Yang, T.-T. Wang, and W. Hsu, *Lab Chip*, **7**, 1330 (2007).
11. S.-K. Fan, C.-P. Chiu, and J.-W. Lin, *Appl. Phys. Lett*., **94**, 164109 (2009).
12. N. Verplanck, E. Galopin, J. C. Camart, and V. Thomy, *Nano Lett*., **7**, 813 (2007).
13. F. Lapoerre and V. Thomy, *Langmuir*, **25**, 6551 (2009).
14. M. Gao, P. Diao, and S. M. Cai, *Thin Solid Films*, **515**, 7162 (2007).
15. J. L. Campbell, M. Breedon, K. Latham, and K. Kalantar-Zadeh, *Langmuir*, **24**, 5091 (2008).
16. A. Tuteja, W. Choi, M. L. Ma, J. M. Mabry, S. A. Mazzella, G. C. Rutledge, G. H. McKinley, and R. E. Cohen, *Science*, **318**, 1618 (2007).
17. V. Bahadur and S. V. Garimella, *Langmuir*, **23**, 4918 (2007).
18. N. A. Patankar, *Langmuir*, **20**, 8209 (2004).
19. X. Gao and L. Jiang, *Nature (London)*, **432**, 36 (2004).
20. M. Vallet, B. Berge, and L. Vovelle, *Polymer*, **37**, 2465 (1996).
21. J. Lee, H. Moon, J. Fowler, T. Schoellhammer, and C.-J. Kim, *Sens. Actuators, A*, **95**, 259 (2002).
22. T. N. Krupenkin, J. A. Taylor, T. M. Schneider, and S. Yang, *Langmuir*, **20**, 3824 (2004).
23. M. S. Dhindsa, N. R. Smith, J. Heikenfeld, P. D. Rack, J. D. Fowlkes, M. J. Doktycz, A. V. Melechko, and M. L. Simpson, *Langmuir*, **22**, 9030 (2006).
24. F. Mugele and J. C. Baret, *J. Phys.: Condens. Matter*, **17**, R705 (2005).
25. N. Verplanck, Y. Coffinier, V. Thomy, and R. Boukherroub, *Nanoscale Res. Lett*., **2**, 577 (2007).
26. S. L. Gras, T. Mahmud, G. Rosengarten, A. Mitchell, and K. Kalantar-Zadeh, *ChemPhysChem*, **8**, 2036 (2007).
27. R. Shamai, D. Andelman, B. Berge, and R. Hayes, *Soft Matter*, **4**, 38 (2008).
28. A. B. Djurisic and Y. H. Leung, *Small*, **2**, 944 (2006).
29. J. M. Wu, C. W. Fang, L. T. Lee, H. H. Yeh, Y. H. Lin, P. H. Yeh, L. N. Tsai, and L. J. Lin, *J. Electrochem. Soc*., **158**, K6 (2011).
30. K. Remashan, Y. S. Choi, S. J. Park, and J. H. Hang, *J. Electrochem. Soc*., **157**, H1121 (2010).
31. C. S. Hsiao, W. L. Kuo, S. Y. Chen, J. L. Shen, C. C. Lin, and S. Y. Cheng, *J. Electrochem. Soc*., **155**, K96 (2008).
32. C. Y. Liu, C. F. Chen, and J. P. Leu, *J. Electrochem. Soc*., **156**, J16 (2009).
33. C. Badre, T. Pauporté, M. Turmin, and D. Lincot, *Nanotechnology*, **18**, 365705 (2007).
34. C. Y. Kuan, M. H. Hon, J. M. Chou, and I. C. Leu, *J. Electrochem. Soc*., **156**, J32 (2009).
35. Y. B. Li, M. J. Zheng, L. Ma, M. Zhong, and W. Z. Shen, *Inorg. Chem.*, **47**, 3140 (2008).
36. E. L. Papadopoulou, A. Pagkozidis, M. Barberoglou, C. Fotakis, and E. Stratakis, *J. Phys. Chem. C*, **114**, 10249 (2010).
37. Y. J. Huang, C. H. Lai, and P. W. Wu, *Electrochem. Solid-State Lett.*, **11**, P20 (2008).
38. Y. H. Huang, C. H. Lai, P. W. Wu, and L. Y. Chen, *J. Electrochem. Soc*., **157**, P18 (2010).
39. Y. J. Huang, C. H. Liao, B. H. Huang, W. Y. Chen, and P. W. Wu, *J. Electrochem. Soc*., **158**, P45 (2011).
40. M. Li, J. Zhai, H. Liu, Y. L. Song, L. Jiang, and D. B. Zhu, *J. Phys. Chem. B*, **107**, 9954 (2003).
41. J. Wu, J. Xia, W. Lei, and B. P. Wang, *Appl. Phys. A*, **99**, 931 (2010).
42. V. Bahadur and S. V. Garimella, *Langmuir*, **24**, 8338 (2008).
43. Z. J. Han, B. K. Tay, C. M. Tan, M. Shakerzadeh, and K. Ostrikov, *ACS Nano*, **3**, 3031 (2009).
44. M. Im, D. H. Kim, J. H. Lee, J. B. Yoon, and Y. K. Choi, *Langmuir*, **26**, 12443 (2010).
45. A. Ahuja, J. A. Taylor, V. Lifton, A. A. Sidorenko, T. R. Salamon, E. J. Lobaton, P. Kolodner, and T. N. Krupenkin, *Langmuir*, **24**, 9 (2008).
46. Z. J. Han, B. K. Tay, M. Shakerzadeh, and K. Ostrikov, *Appl. Phys. Lett.*, **94**, 223106 (2009).
47. J. Rousset, E. Saucedo, and D. Lincot, *Chem. Mater*., **21**, 534 (2009).
48. O. Ozdemir, S. I. Karakashev, A. V. Nguyen, and J. D. Miller, *Minerals Eng.*, **22**, 263 (2009).
49. E. L. Papadopoulou, M. Barberoglou, V. Zorba, A. Manousaki, A. Pagkozidis, E. Stratakis, and C. Fotakis, *J. Phys. Chem. C*, **113**, 2891 (2009).
50. M. Barberoglou, V. Zorba, A. Pagozidis, C. Fotakis, and E. Stratakis, *Langmuir*, **26**, 13007 (2010).
51. P. Brunet, F. Lapierre, V. Thomy, V. Coffinier, and R. Boukherroub, *Langmuir*, **24**, 11203 (2008).
52. F. Lapierre, V. Thomy, Y. Coffinier, R. Biossey, and R. Boukherroub, *Langmuir*, **25**, 6551 (2009).